Robust Electromagnetic Pose Estimation for Robotic Applications

Harald Gietler, Habib Ammari, and Hubert Zangl

***Abstract*— A wireless electromagnetic field-based sensor system is proposed, which enables the tracking of moving objects, e.g., drones. The gathered up to 6-degrees of freedom information is complementary to existing sensing principles, e.g., global positioning system (GPS) or vision-based systems. In addition, it can be used for stand-alone navigation or noninvasive localization of medical devices inside the human body. The sensor system is comprised of an exciter and a sensor. The exciter can be mounted on a moving robot and generates an electromagnetic field. The field is measured by the sensor, and subsequently, the pose of the exciter with respect to the sensors' pose is estimated. Conductive objects in the vicinity of the sensor alter the measured magnetic field due to the induced eddy currents. In general, unmanned aerial vehicles or wheeled robots mainly consist of conductive materials, which cause a significant estimation error. This article introduces an interference-aware electromagnetic near-field-based pose estimation approach. Specifically, the change in the magnetic field due to close conductive and ferromagnetic objects is modeled. Iterative numerical solutions of Maxwell's equations, based on, e.g., finite-element method, are avoided. Instead, an analytic expression of the change in the magnetic field due to present eddy currents is given. The advantages of the proposed concept for model-based low-complexity pose estimation concepts are shown using an extended Kalman filter. It is observed that the tracking performance using the introduced model outperforms the traditional model in eddy current scenarios significantly.**

***Index Terms*— Computational electromagnetics, eddy currents, Kalman filters (KFs), magnetic field measurement, pose estimation.**

I. Introduction

ALONG with the growing number of autonomous mobile platforms, the demand of accurate localization approaches for navigational tasks increases. Recent research focuses on indoor navigation, a global positioning system (GPS)-denied environment, using the visual and inertial sensors for pose estimation [1]. However, their accuracy decreases when approaching objects. Reasons are, e.g., motion blur and low overlap between consecutive images. Alternatively, ultra wide band (UWB) modules have been used for indoor localization enabling high accuracy [2] and the capability of data transmission at the same time. However, a direct line of sight is necessary between the transmitter and the receiver to maintain accuracy [3], [4]. This issue is addressed by placing redundant UWB modules, which increases the chance to cover the targeted object. Alternatively, electromagnetic field-based sensors can be used to estimate the pose of the mobile platform [5], [6]. Recently, magnetic field-based sensors were proposed as the noninvasive localization method for the miniature medical device in human bodies [7]. Electromagnetic field-based approaches do not rely on direct line of sight and do not drift over time. The drawback is the limited range, but usually, the accuracy increases with the decreasing distance. Thus, they are beneficial to the robotics field [8], [9] especially when using them complementary to existing systems such as visual-inertial odometry (VIO). This article introduces a robust electromagnetic field-based localization concept. It is comprised of an electromagnetic field emitter and a magnetic field sensor. The emitter can be positioned on any moving platform, e.g., a robot-arm end-effector or a unmanned aerial vehicle (UAV). The sensor is supposed to have a fixed pose and its measurement data are used to estimate the relative pose of the field source. It is well known that conductive materials in the vicinity of the field alter the field distribution. This is caused by the induced eddy currents that create an additional electromagnetic field, which interacts with the original field. The introduced concept is able to suppress the influence of the known conductive materials such as the moving platform itself. This significantly increases the robustness of the approach especially for highly conductive materials, e.g., metals. Note that iterative numerical solving of Maxwell's equations is avoided. Instead, the change in the magnetic field due to the interference is explicitly formulated [10]. The accuracy of the formulation is verified by comparing it with a classical finite element method (FEM)-based solution. Due to its low computational complexity, the concept is especially useful for real-time applications. This is ultimately showcased by using an extended Kalman filter (EKF)-based tracking approach. A comparison between the traditional model that assumes surrounding air and the extended model for conductive and ferromagnetic objects close to the sensor systems is carried out. The results substantiate the need for models considering the electromagnetic interferences (EMIs) caused by parasitic eddy currents. Finally, an investigation of the algorithmic complexity is reported, which pronounces the applicability for real-time devices.

II. System Model

The proposed concept consists of a freely movable alternating magnetic field source (emitter), e.g., attached to a UAV,

Manuscript received June 13, 2019; revised September 19, 2019; accepted September 22, 2019. Date of publication October 3, 2019; date of current version June 9, 2020. This work was supported by the Swiss National Science Foundation under Grant 200021–172483. The Associate Editor coordinating the review process was Vedran Bilas. *(Corresponding author: Harald Gietler.)*

H. Gietler and H. Zangl are with the Institute of Smart Systems Technologies, University of Klagenfurt, 9020 Klagenfurt, Austria (e-mail: harald.gietler@aau.at).

H. Ammari is with the Department of Mathematics, Swiss Federal Institute of Technology in Zürich (ETHZ), 8092 Zürich, Switzerland.

Color versions of one or more of the figures in this article are available online at http://ieeexplore.ieee.org.

Digital Object Identifier 10.1109/TIM.2019.2945494

and a magnetic field sensor arrangement with a fixed position and an attitude, e.g., on the ground. Ideally, the emitter consists of three-point dipole sources with orthogonal magnetic dipole moments. A manufacturable system could be a stack of small orthogonally placed coils, which can be approximated by a dipole model. The approximation is valid in certain limits described in [11]. Alternatively, each coil can be modeled as a stack of magnetic point sources rather than just multiplying the magnetic dipole moment with the number of turns. Such a coil structure may efficiently be driven using rectangular waveforms and employing parallel resonant circuitries. The complementary magnetic field sensor could also consist of three orthogonally placed pick-up coils to serve for all three spatial axes. Often, it is assumed that placing the emitter on the moving platform is disadvantageous in terms of energy consumption. This is not always true, especially when low-noise amplifiers are used on the receiver side. They often consume more energy than the transmitter circuitry. On the contrary, placing the receiver on the robot may cause EMI issues. Note that the source of interferences, e.g., motors, can be very close to the receiver. When the transmitter is far away, the EMIs could be critical. In addition, it is easier to provide computational power at the ground station, which is required on the receiver side. Hence, the transmitter is placed on the moving platform and the receiver is located at the base station.

The first-field analysis neglects the emitter-carrying platform, and the surrounding space is assumed to be air. The magnetic field strength at the sensor position $\mathbf{x}_r$ is then given by [12]

$$\mathbf{H}_0(\mathbf{r},\mathbf{m}) = \begin{bmatrix} H_x \\ H_y \\ H_z \end{bmatrix} = \frac{1}{4\pi}\left(\frac{3\mathbf{r}(\mathbf{m}\cdot\mathbf{r})}{|\mathbf{r}|^5} - \frac{\mathbf{m}}{|\mathbf{r}|^3}\right). \tag{1}$$

The quantities $\mathbf{r} = \mathbf{x}_r - \mathbf{x}_s$, $\mathbf{m}$, and μ_0 denote the relative position with respect to the emitter, the magnetic moment of the emitter, and the permeability of free space, respectively. An understandable visualization of the geometrical dependences is shown in Fig. 1. If the attitude of the mobile platform changes, $\mathbf{r}$ remains the same, whereas $\mathbf{m}$ would be altered. Therefore, the magnetic dipole moment can be used to model the attitude of the emitter and more generic the attitude of the mobile platform. Reformulating the magnetic dipole moment yields

$$\mathbf{m} = \mathbf{R}\mathbf{m}' \tag{2}$$

where $\mathbf{m}'$ is the magnetic dipole moment in initial situation and $\mathbf{R} \in \mathbb{R}^{3\times3}$ is a rotational matrix, with $\mathbf{x}_s$ being the center of rotation. $\mathbf{R}$ is defined by the rotation angles $\boldsymbol{\theta} \in \mathbb{R}^3$ and the rotation sequence

$$\mathbf{R} = \mathbf{R}_z\mathbf{R}_y\mathbf{R}_x \tag{3}$$

where $\mathbf{R}_z$, $\mathbf{R}_y$, and $\mathbf{R}_x$ are given by

$$\mathbf{R}_z = \begin{bmatrix} \cos\theta_3 & -\sin\theta_3 & 0 \\ \sin\theta_3 & \cos\theta_3 & 0 \\ 0 & 0 & 1 \end{bmatrix}, \quad \mathbf{R}_y = \begin{bmatrix} \cos\theta_2 & 0 & \sin\theta_2 \\ 0 & 1 & 0 \\ -\sin\theta_2 & 0 & \cos\theta_2 \end{bmatrix}$$

$$\mathbf{R}_x = \begin{bmatrix} 1 & 0 & 0 \\ 0 & \cos\theta_1 & -\sin\theta_1 \\ 0 & \sin\theta_1 & \cos\theta_1 \end{bmatrix}. \tag{4}$$

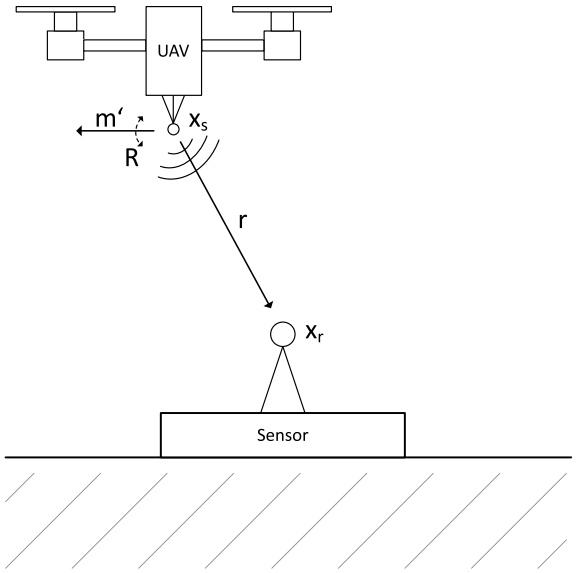

Fig. 1. Schematic view of the proposed system. The electromagnetic field emitter is mounted on the mobile platform, i.e., UAV, whereas the sensor is attached to the ground. The relative position and orientation of the emitter are of interest.

Suppose the magnitude of the magnetic moment is known, then the magnetic field strength at any observation point is described by 6-degrees of freedom (DOF), i.e., the space vector pointing from the emitter to the point of observation and the attitude of the emitter. For some applications, partial information about the pose already exists, which can be used to reduce the model complexity.

Independent of the field model, different kinds of magnetic sensors can be used to measure the local magnetic field. A common way to measure alternating magnetic fields is pick-up coils [13], [14]. Faraday's law links the local magnetic field strength to the induced electromagnetic force. For a homogeneous magnetic field in the cross section of an air-cored solenoid, the electromagnetic force is given by [15]

$$V = -\mu_0\ N\mathbf{A}\cdot\frac{\delta\mathbf{H}}{\delta t} \tag{5}$$

where N is the number of windings and $\mathbf{A}$ represents the area of the cross section of the coil. For a nonhomogeneous magnetic field, e.g., dipole field, this can still be a good approximation depending on the location of the point of observation. The taken measurements are the basis for pose estimation. Due to the model order, a single observation is not sufficient to get an accurate estimate. Therefore, a number of either sensors or emitters are required.

III. Tracking of a Mobile Target

This section presents an approach to estimate both the location and orientation of the target. A widely used approach to track system states is the Kalman Filter (KF). It produces an optimal estimator for linear systems with Gaussian noise. The EKF is the generalization of the KF to nonlinear dynamical systems. Note that the EKF does not produce an optimal estimator anymore. Although it remains robust with respect to

noise and is computationally cheap, which makes it suitable for real-time applications.

A. System-State Observation

In general, the dynamics of the employed robots can be used to model the system states, i.e., pose and velocities. Here, the target dynamics are modeled in a generic fashion in order to be independent of specific devices. A general external driving acceleration that has the form of white noise is assumed to affect the position of the target. The velocity $(\mathbf{V}(\tau))_{\tau\in\mathbb{R}^+}$ of the target is given in terms of a 3-D Brownian motion, also known as Wiener process $(\mathbf{W}_v(\tau))_{\tau\in\mathbb{R}^+}$, and its position $(\mathbf{Z}(\tau))_{\tau\in\mathbb{R}^+}$ is given by the integral over the Brownian motion. The increments of $\mathbf{W}_v$, e.g., $\mathbf{W}_v(t) - \mathbf{W}_v(s)$ with $0 \leq s < t$, are statistically independent and distributed as $\mathcal{N}(0, t-s)$. The stochastic differential equation linking the random acceleration and the velocity term can be solved, as shown in [16]

$$\mathbf{V}(\tau) = \mathbf{V}_0 + \boldsymbol{\sigma}_v \mathbf{W}_v(\tau), \qquad \mathbf{Z}(\tau) = \mathbf{Z}_0 + \int_0^\tau \mathbf{V}(s)ds. \tag{6}$$

Note that $\mathbf{V}_0 = \mathbf{V}(0)$ and $\mathbf{Z}_0 = \mathbf{Z}(0)$ are constant vectors and denote the initial velocity and position of the object, respectively. The angular acceleration of the target is subject to independent white noise, so that the angular velocity $(\boldsymbol{\Omega}(\tau))_{\tau\in\mathbb{R}^+}$ is given by means of a 3-D Brownian motion $(\mathbf{W}_\omega(\tau))_{\tau\in\mathbb{R}^+}$

$$\boldsymbol{\Omega}(\tau) = \boldsymbol{\Omega}_0 + \boldsymbol{\sigma}_\omega \mathbf{W}_\omega(\tau), \qquad \boldsymbol{\Theta}(\tau) = \boldsymbol{\Theta}_0 + \int_0^\tau \boldsymbol{\Omega}(s)ds. \tag{7}$$

Here, $\boldsymbol{\Omega}_0 = \boldsymbol{\Omega}(0)$ and $\boldsymbol{\Theta}_0 = \boldsymbol{\Theta}(0)$ are constant vectors and denote the initial angular velocity and orientation of the target, respectively. The target can be observed at discrete times $t\Delta\tau,\ t \in \mathbb{N}$, with time step $\Delta\tau$. Furthermore, we denote the system states at time step $t\Delta\tau$ as $\mathbf{v}_t$, $\mathbf{z}_t$, $\boldsymbol{\omega}_t$, and $\boldsymbol{\theta}_t$. They can be represented using the recursive relations

$$\begin{aligned}
\mathbf{v}_t &= \mathbf{v}_{t-1} + \boldsymbol{\alpha}_t \\
\boldsymbol{\alpha}_t &= \boldsymbol{\sigma}_v(\mathbf{W}_v(t\Delta\tau) - \mathbf{W}_v((t-1)\Delta\tau)) \\
\mathbf{z}_t &= \mathbf{z}_{t-1} + \mathbf{v}_{t-1}\Delta\tau + \boldsymbol{\beta}_t \\
\boldsymbol{\beta}_t &= \boldsymbol{\sigma}_v \int_{(t-1)\Delta\tau}^{t\Delta\tau} (\mathbf{W}_v(\mathbf{s}) - \mathbf{W}_v((t-1)\Delta\tau))ds \\
\boldsymbol{\omega}_t &= \boldsymbol{\omega}_{t-1} + \boldsymbol{\gamma}_t \\
\boldsymbol{\gamma}_t &= \boldsymbol{\sigma}_\omega(\mathbf{W}_\omega(t\Delta\tau) - \mathbf{W}_\omega((t-1)\Delta\tau)) \\
\boldsymbol{\theta}_t &= \boldsymbol{\theta}_{t-1} + \mathbf{v}_{t-1}\Delta\tau + \boldsymbol{\delta}_t \\
\boldsymbol{\delta}_t &= \boldsymbol{\sigma}_\omega \int_{(t-1)\Delta\tau}^{t\Delta\tau} (\mathbf{W}_\omega(\mathbf{s}) - \mathbf{W}_\omega((t-1)\Delta\tau))ds.
\end{aligned} \tag{8}$$

The increments of the Brownian motions are independent of each other and are summarized in

$$\mathbf{U}_t = \begin{bmatrix} \boldsymbol{\alpha}_t \\ \boldsymbol{\beta}_t \\ \boldsymbol{\gamma}_t \\ \boldsymbol{\delta}_t \end{bmatrix}. \tag{9}$$

The instances of $\mathbf{U}_t$ are independent and identically distributed with the multivariate normal distribution with zero mean and covariance matrix $\boldsymbol{\Sigma}$ given by

$$\boldsymbol{\Sigma} = \Delta\tau \begin{bmatrix} \boldsymbol{\sigma}_v^2\mathbf{I} & \frac{\boldsymbol{\sigma}_v^2}{2}\Delta\tau\mathbf{I} & \mathbf{0} & \mathbf{0} \\ \frac{\boldsymbol{\sigma}_v^2}{2}\Delta\tau\mathbf{I} & \frac{\boldsymbol{\sigma}_v^2}{3}\Delta\tau^2\mathbf{I} & \mathbf{0} & \mathbf{0} \\ \mathbf{0} & \mathbf{0} & \boldsymbol{\sigma}_\omega^2\mathbf{I} & \frac{\boldsymbol{\sigma}_\omega^2}{2}\Delta\tau\mathbf{I} \\ \mathbf{0} & \mathbf{0} & \frac{\boldsymbol{\sigma}_\omega^2}{2}\Delta\tau\mathbf{I} & \frac{\boldsymbol{\sigma}_\omega^2}{3}\Delta\tau^2\mathbf{I} \end{bmatrix} \tag{10}$$

where $\mathbf{I}$ represents the 3-D identity matrix. The covariance matrix can be computed using Ito's lemma to account for the stochastic integrals [17]. The state vector

$$\mathbf{X}_t = \begin{bmatrix} \mathbf{v}_t \\ \mathbf{z}_t \\ \boldsymbol{\omega}_t \\ \boldsymbol{\theta}_t \end{bmatrix} \tag{11}$$

is linearly propagating, satisfying

$$\mathbf{X}_t = \mathbf{F}\mathbf{X}_{t-1} + \mathbf{U}_t, \quad \mathbf{F} = \begin{bmatrix} \mathbf{I} & \mathbf{0} & \mathbf{0} & \mathbf{0} \\ \Delta\tau\mathbf{I} & \mathbf{I} & \mathbf{0} & \mathbf{0} \\ \mathbf{0} & \mathbf{0} & \mathbf{I} & \mathbf{0} \\ \mathbf{0} & \mathbf{0} & \Delta\tau\mathbf{I} & \mathbf{I} \end{bmatrix}. \tag{12}$$

The magnetic field observation made at time t using (1) is denoted as $\mathbf{V}_t$. The magnetic field observation is also subject to additive noise $\mathbf{W}_t$. Note that the system state $\mathbf{z}_t$ corresponds to the position of the magnetic field source $\mathbf{x}_s$ and the system state $\boldsymbol{\theta}_t$ corresponds to the orientation of the magnetic dipole moment defined in (2)–(4). The velocity vectors $\mathbf{v}_t$ and $\boldsymbol{\omega}_t$ do not contribute to (1). To highlight the dependence upon $\mathbf{z}_t, \boldsymbol{\theta}_t$, the nonlinear function $\mathbf{h}$ is introduced, which corresponds to (1). Then, together with (12), the system state and observation equations are given by

$$\mathbf{X}_t = \mathbf{F}\mathbf{X}_{t-1} + \mathbf{U}_t \tag{13}$$

$$\mathbf{V}_t = \mathbf{h}(\mathbf{z}_t, \boldsymbol{\theta}_t) + \mathbf{W}_t. \tag{14}$$

B. EKF

This section summarizes the well-known EKF approach [18], [19]. Consider a nonlinear dynamical system with the state propagation function f_t' depending on the system states X_{t-1}' and process noise $W_t' \sim \mathcal{N}(0, Q_t\prime)$ and the observation equation h_t' depending on X_t' and measurement noise $V_t' \sim \mathcal{N}(0, R_t')$

$$X_t' = f_t'(X_{t-1}', W_t') \tag{15}$$

$$Y_t' = h_t'(X_t', V_t'). \tag{16}$$

The functions f_t', h_t' are nonlinear and differentiable. In general, nothing can be said about the conditional distribution $X_t'|Y_{1:t}'$ due to the nonlinearity. The EKF calculates an approximation of the conditional expectation by an appropriate linearization of the state transition and observation model. Due to the approximation, the resulting algorithm is not optimal in the least-squares sense. Let F_X' and F_W' be the partial derivatives of f' with respect to system state and process noise, respectively. Furthermore, let H_X' and H_V' be the partial derivatives of h' with respect to system state

and measurement noise, respectively. The EKF algorithm is summarized in the following.

1) *Initialization:*

$$\hat{x}'_{0|0} = E\left[X'_0\right], \quad P'_{0|0} = cov\left(X'_0\right). \tag{17}$$

2) *Prediction:*

$$\hat{x}'_{t|t-1} = f'\left(\hat{x}'_{t-1|t-1}, 0\right) \tag{18}$$
$$Y'_{e,t} = Y'_t - h'\left(\hat{x}'_{t|t-1}, 0\right) \tag{19}$$
$$P'_{t|t-1} = F'_X P'_{t-1|t-1} F'^T_X + F'_W Q'_t F'^T_W. \tag{20}$$

3) *Update:*

$$S'_t = H'_X P'_{t|t-1} H'^T_X + H'_V R'_t H'^t_V \tag{21}$$
$$K'_t = P'_{t|t-1} H'^T_X S'^{-1}_t \tag{22}$$
$$\hat{x}'_{t|t} = \hat{x}'_{t|t-1} + K'_t Y'_{e,t} \tag{23}$$
$$P'_{t|t} = \left(I - K'_t H'_X\right) P'_{t-1|t-1}. \tag{24}$$

C. Tracking Experiments

In this section, the performance of the EKF-based tracking is investigated. As mentioned, a number of unique measurements are required due to the model complexity. Therefore, three emitters and one sensor are used. The sensor is measuring the 3-D field at a known spatial point. The emitters are static to each other. However, in a global coordinate frame, the vector between the emitters is not static due to the rotation of the object. Without the presence of rotation, the distance between the first emitter s_1 and the second emitter s_2 is given by $\mathbf{p}_{12} = [0.05,\ 0.05,\ 0.05]^T$. The distance between the first and the third emitter s_3 is given by $\mathbf{p}_{13} = [-0.02,\ 0.03,\ 0.02]^T$. The position of s_1 is used as target position $\mathbf{x}_s$ following the trajectory simulated according to (8). A period of 20 s using $\Delta\tau = 0.1$ s with parameters $\boldsymbol{\sigma}_\upsilon = 0.01, \boldsymbol{\sigma}_\omega = 0.1$ and initial state $\mathbf{X}_0 = [\mathbf{v}_0,\ \mathbf{z}_0,\ \boldsymbol{\omega}_0,\ \boldsymbol{\theta}_0]$ is simulated

$$\mathbf{v}_0 = [0.01,\ 0,\ -0.005]^T, \quad \mathbf{z}_0 = [0.2,\ -0.2,\ 0.3]^T$$
$$\boldsymbol{\omega}_0 = [0,\ 0,\ 0]^T, \quad \boldsymbol{\theta}_0 = \left[0.02,\ -0.05,\ \frac{\pi}{4}\right]^T.$$

The measurement data $\mathbf{V}_t$ are generated first, calculating the magnetic field using (1) and then adding white noise. The receiver $\mathbf{x}_r$ is located in the origin. Note that the emitters are used in a time-multiplexed fashion; thus, only one emitter is transmitting at any instant in time. In addition, the magnetic dipole moment of each emitter is 1 Am^2, and they point toward orthogonal directions. The initial guess of $\mathbf{X}_0$ for the EKF is $\hat{\mathbf{X}}_0 = [\hat{\mathbf{v}}_0,\ \hat{\mathbf{z}}_0,\ \hat{\boldsymbol{\omega}}_0,\ \hat{\boldsymbol{\theta}}_0]$ given by

$$\hat{\mathbf{v}}_0 = [0,\ 0,\ 0]^T, \quad \hat{\mathbf{z}}_0 = [0.05,\ -0.1,\ 0.4]^T$$
$$\hat{\boldsymbol{\omega}}_0 = [0,\ 0,\ 0]^T, \quad \hat{\boldsymbol{\theta}}_0 = [0,\ 0,\ 1]^T.$$

Note that (13) is linear; therefore, in order to apply the EKF, only (14) needs to be linearized. This can be done by calculating the partial derivatives of $\mathbf{h}$ with respect to $\mathbf{X}_t$. The tracking performance of the EKF in terms of position $\hat{\mathbf{x}}_s$ is shown in Fig. 2 and in terms of orientation $\hat{\boldsymbol{\theta}}$ is reported in Fig. 3. It can be seen that the true system states can be found, despite the poor initial guess. The process noise covariance is given by (10). The initial state propagation covariance is set to $0.1 \cdot \mathbf{I}$, and the measurement noise is additive white Gaussian noise (AWGN) with a variance of 10^{-4}. This results in an average signal-to-noise ratio (SNR) of approximately 30–40 dB at 1-m distance. The measurement noise is added to all the components of the field. For the dominant parts of the field, it appears to be quite small. Despite the parts with small amplitude where it is significant,

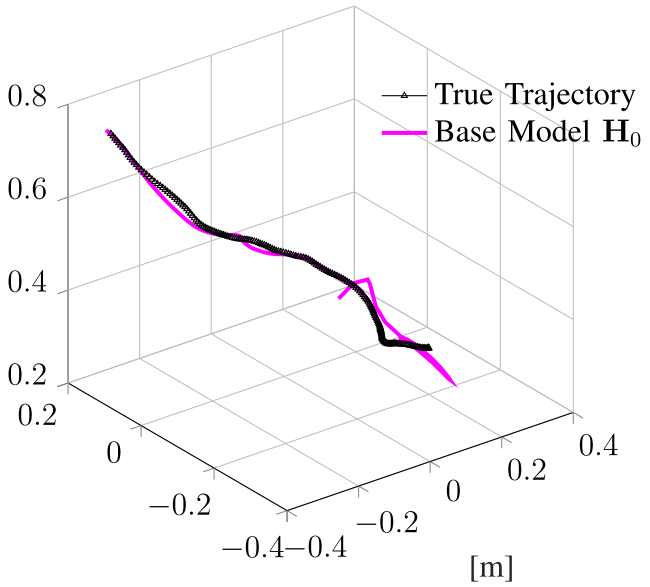

Fig. 2. Magnetic field source is moving along a random trajectory, indicated with black markers, driven by Brownian motion. The EKF estimates the trajectory shown as magenta waveform. The algorithm is able to identify the true states, despite its poor initial guess.

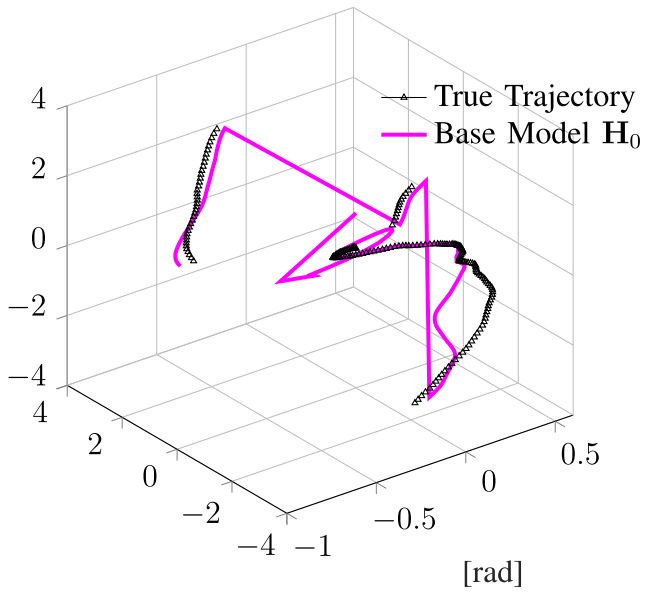

Fig. 3. While moving along the trajectory, the orientation of the magnetic field source is changing by means of a 3-D Brownian motion. The true orientation is indicated with black markers, whereas the estimated orientation is shown as a magenta waveform. Note that the x-value, y-value, and z-value represent the rotation around the x-, y-, and z-axes, respectively.

TABLE I
MSE IS CARRIED OUT FOR DIFFERENT MEASUREMENT NOISE LEVELS

Measurement Noise Variance σ^2 $(\frac{\mathrm{A}^2}{\mathrm{m}^2})$	10^{-1}	10^{-2}	10^{-3}	10^{-4}	10^{-5}
MSE Base Model $\mathbf{H}_0$ (m^2)	0.1210	0.0518	0.0144	0.0028	0.0010

an SNR at 1-m distance can drop below 0 dB for the individual components. The tracking accuracy decays with the increasing distance to the receiver. This is explained by the decreasing SNR of the measured magnetic field. Jumps in the orientation result plot are due to the restriction of the angle to $-\pi \leq \boldsymbol{\theta} < \pi$. The experiment is repeated a hundred times and the average mean squared error (mse) is reported in Table I. Here, divergence of the EKF is detected by watching the estimated position. When the distance between the receiver and the estimate becomes greater than 2 m, the experiment is stopped. The mse is based on the distance between the estimate and the true position ($|\mathbf{z}_t - \hat{\mathbf{z}}_t|$). Five different measurement noise levels are carried out, and the results are compared.

IV. EDDY CURRENT MODEL

The previous chapter showed that a stack of moving magnetic field sources can be tracked using an EKF. However, conductive objects in the vicinity of the sensor are not considered and may distort the pose estimation, because the magnetic field is altered and is not accurately modeled by (1) anymore. Often the carrier of the emitter, e.g., UAV or wheeled robot, is made of conductive materials. This chapter introduces a methodology to suppress the influence of those known conductive objects. Suppose that there is an electromagnetic inclusion in $\mathbb{R}^3$ of the form B, where B is a bounded, smooth domain. Let the constant quantities $\mu_\star$ and $\sigma_\star$ denote the permeability and conductivity of the inclusion. The piecewise constant magnetic permeability and electric conductivity are given by

$$\mu_a = \begin{cases} \mu_\star & \text{in } B \\ \mu_0 & \text{in } B^c = \mathbb{R}^3 \setminus B \end{cases} \qquad \sigma_a = \begin{cases} \sigma_\star & \text{in } B \\ \sigma_0 & \text{in } B^c. \end{cases} \tag{25}$$

Let $(\mathbf{E}_a, \mathbf{H}_a)$ denote the eddy current fields in the presence of the electromagnetic inclusion B and a source current $\mathbf{J}_0$ located outside the inclusion. It is supposed that $\mathbf{J}_0$ is divergence free $\nabla \cdot \mathbf{J}_0 = 0$ in $\mathbb{R}^3$. The fields $(\mathbf{E}_a, \mathbf{H}_a)$ are the solutions of the following eddy current equations:

$$\begin{cases} \nabla \times \mathbf{E}_a = i\omega\mu_a \mathbf{H}_a & \text{in } \mathbb{R}^3 \\ \nabla \times \mathbf{H}_a = \sigma_a \mathbf{E}_a + \mathbf{J}_0 & \text{in } \mathbb{R}^3 \\ \mathbf{E}_a(\mathbf{x}) = \mathcal{O}(|\mathbf{x}|^{-1}), \quad \mathbf{H}_a(\mathbf{x}) = \mathcal{O}(|\mathbf{x}|^{-1}) & \text{as } |\mathbf{x}| \to \infty. \end{cases} \tag{26}$$

Commonly, FEM-based simulation environments are used to solve (26) for $\mathbf{H}_a$. Those approaches come with high computational cost and are often not applicable in low-power real-time devices. In the applied mathematics community, the change in magnetic field $\tilde{\mathbf{H}}_a = \mathbf{H}_a - \mathbf{H}_0$ due to the presence of the object B is explicitly expressed given by (27). The mathematical proof is conducted in [10]

$$\tilde{\mathbf{H}}_a(\mathbf{x}_r) = \int_B \nabla_{\mathbf{x}_r} G(\mathbf{x}_r, \mathbf{y}) \times \nabla_{\mathbf{y}} \times \tilde{\mathbf{H}}_a(\mathbf{y}) d\mathbf{y} + \left(1 - \frac{\mu_\star}{\mu_0}\right) \times \int_B (\mathbf{H}_a(\mathbf{y}) \cdot \nabla_{\mathbf{y}}) \nabla_{\mathbf{x}_r} G(\mathbf{x}_r, \mathbf{y}) d\mathbf{y}. \tag{27}$$

Here, $\mathbf{x}_r$ denotes the point of observation, where $\mathbf{x}_r \in B^c$. The scalar function $G(\mathbf{x}_r, \mathbf{y})$ represents the fundamental solution of the Laplace equation given by

$$G(\mathbf{x}_r, \mathbf{y}) = \frac{1}{4\pi |\mathbf{x}_r - \mathbf{y}|}. \tag{28}$$

In Sections IV-A–IV-D, it is shown that this formula is especially useful for objects that are static with respect to the emitter. In such a situation, the curl of $\tilde{\mathbf{H}}_a(\mathbf{y})$ as well as the field $\mathbf{H}_a(\mathbf{y})$ are constant.

A. Numerical Experiments and Verification

This section investigates the accuracy of the formula given in (27) by comparing it with the classical FEM-based approach. Therefore, a cube made of copper is centered at $[0\ 0\ 0.15]^T$. Its electrical conductivity and edge length are given by $\sigma_\star = 59.9 \times 10^6$ S/m and 0.05 m, respectively. The used magnetic permeability is $\mu_\star = \mu_0 = 4\pi \times 10^{-7}$ H/m. The first emitter is located at $[0\ 0\ 0.2]^T$. The distances to the second and the third emitter are reused from Section III-C, given by $\mathbf{p}_{12}$ and $\mathbf{p}_{13}$. The corresponding dipole moments are

$$\mathbf{m}_0 = \begin{bmatrix} 0 \\ 0 \\ 0.01 \end{bmatrix} \quad \mathbf{m}_1 = \begin{bmatrix} 0 \\ 0.01 \\ 0 \end{bmatrix} \quad \mathbf{m}_2 = \begin{bmatrix} 0.01 \\ 0 \\ 0 \end{bmatrix} \quad \mathrm{Am}^2.$$

The point of observation $\mathbf{x}_r$ is located at $[0.05\ 0.05\ 0.2]^T$. As a reference, a commercial FEM-based software kit is used [20]. The simulation runs once in the presence and once in the absence of the copper cube and calculates the magnetic field at $\mathbf{x}_r$. The magnetic field difference represents the reference result $\tilde{\mathbf{H}}_r$. It is worth noting that boundary conditions regarding the simulation environment border are avoided by extending the mesh until the field drops below the numerical boundary. The used excitation frequency is 450 kHz. Consequently, the near-field region is around 666 m and field-propagation phase shifts are negligibly small for short distances. In addition, the penetration depth of objects with low conductivity such as desks and concrete walls is large, and they do not shield the field. This excitation frequency is used throughout the article. The explicit formula (27) is used to obtain a comparative result. The field curl difference $\nabla_{\mathbf{y}} \times \tilde{\mathbf{H}}_a(\mathbf{y})$ and the magnetic field $\mathbf{H}_a(\mathbf{y})$ are precomputed using the presented FEM environment. The remaining parts of (27) are analytically evaluated. Note that the object is

TABLE II
COMPARISON OF THE FEM-BASED SOLUTION WITH THE EXPLICIT FORMULA. THE USED OBJECT PARAMETERS ARE $\sigma_\star = 59.9 \times 10^6$ S/m AND $\mu_\star = \mu_0 = 4\pi \times 10^{-7}$ H/m

		x-component	y-component	z-component
Emitter 1	FEM solution $\tilde{\mathbf{H}}_r$	$230.310\ \frac{\mathrm{mA}}{\mathrm{m}}$	$217.780\ \frac{\mathrm{mA}}{\mathrm{m}}$	$-123.660\ \frac{\mathrm{mA}}{\mathrm{m}}$
	Explicit solution $\tilde{\mathbf{H}}_a$	$227.340\ \frac{\mathrm{mA}}{\mathrm{m}}$	$223.630\ \frac{\mathrm{mA}}{\mathrm{m}}$	$-119.120\ \frac{\mathrm{mA}}{\mathrm{m}}$
Emitter 2	FEM solution $\tilde{\mathbf{H}}_r$	$17.742\ \frac{\mathrm{mA}}{\mathrm{m}}$	$4.450\ \frac{\mathrm{mA}}{\mathrm{m}}$	$-4.174\ \frac{\mathrm{mA}}{\mathrm{m}}$
	Explicit solution $\tilde{\mathbf{H}}_a$	$17.821\ \frac{\mathrm{mA}}{\mathrm{m}}$	$4.260\ \frac{\mathrm{mA}}{\mathrm{m}}$	$-3.628\ \frac{\mathrm{mA}}{\mathrm{m}}$
Emitter 3	FEM solution $\tilde{\mathbf{H}}_r$	$-19.831\ \frac{\mathrm{mA}}{\mathrm{m}}$	$-10.634\ \frac{\mathrm{mA}}{\mathrm{m}}$	$-25.090\ \frac{\mathrm{mA}}{\mathrm{m}}$
	Explicit solution $\tilde{\mathbf{H}}_a$	$-19.287\ \frac{\mathrm{mA}}{\mathrm{m}}$	$-9.726\ \frac{\mathrm{mA}}{\mathrm{m}}$	$-26.752\ \frac{\mathrm{mA}}{\mathrm{m}}$

TABLE III
COMPARISON OF THE FEM-BASED SOLUTION WITH THE EXPLICIT FORMULA. THE USED OBJECT PARAMETERS ARE $\sigma_\star = 0.1 \times 10^6$ S/m AND $\mu_\star = 100 \cdot \mu_0 = 4\pi \times 10^{-5}$ H/m

		x-component	y-component	z-component
Emitter 1	FEM solution $\tilde{\mathbf{H}}_r$	$(-248.620 + 91.751\mathrm{i})\ \frac{\mathrm{mA}}{\mathrm{m}}$	$(-245.780 + 88.301\mathrm{i})\ \frac{\mathrm{mA}}{\mathrm{m}}$	$(379.540 - 71.226\mathrm{i})\ \frac{\mathrm{mA}}{\mathrm{m}}$
	Explicit solution $\tilde{\mathbf{H}}_a$	$(-247.620 + 90.374\mathrm{i})\ \frac{\mathrm{mA}}{\mathrm{m}}$	$(-247.240 + 88.652\mathrm{i})\ \frac{\mathrm{mA}}{\mathrm{m}}$	$(373.891 - 69.934\mathrm{i})\ \frac{\mathrm{mA}}{\mathrm{m}}$
Emitter 2	FEM solution $\tilde{\mathbf{H}}_r$	$(13.957 + 8.412\mathrm{i})\ \frac{\mathrm{mA}}{\mathrm{m}}$	$(-228.560 + 2.317\mathrm{i})\ \frac{\mathrm{mA}}{\mathrm{m}}$	$(-1.376 - 2.981\mathrm{i})\ \frac{\mathrm{mA}}{\mathrm{m}}$
	Explicit solution $\tilde{\mathbf{H}}_a$	$(13.712 + 8.236\mathrm{i})\ \frac{\mathrm{mA}}{\mathrm{m}}$	$(-232.007 + 2.268\mathrm{i})\ \frac{\mathrm{mA}}{\mathrm{m}}$	$(-1.643 - 2.874\mathrm{i})\ \frac{\mathrm{mA}}{\mathrm{m}}$
Emitter 3	FEM solution $\tilde{\mathbf{H}}_r$	$(-86.642 - 10.840\mathrm{i})\ \frac{\mathrm{mA}}{\mathrm{m}}$	$(57.967 - 6.754\mathrm{i})\ \frac{\mathrm{mA}}{\mathrm{m}}$	$(-398.010 - 11.367\mathrm{i})\ \frac{\mathrm{mA}}{\mathrm{m}}$
	Explicit solution $\tilde{\mathbf{H}}_a$	$(-86.256 - 10.581\mathrm{i})\ \frac{\mathrm{mA}}{\mathrm{m}}$	$(59.167 - 6.668\mathrm{i})\ \frac{\mathrm{mA}}{\mathrm{m}}$	$(-395.791 - 11.422\mathrm{i})\ \frac{\mathrm{mA}}{\mathrm{m}}$

statically linked to the field emitter. Consequently, the field and its curl at the object are independent of the global position and orientation. Hence, it is only required to be calculated once, independent of the relative pose with respect to the receiver.

As shown in Table II, the classical FEM-based approach and (27) obtain similar results. The minor discrepancies are mostly explained by numerical inaccuracies. It is worth noting that the magnetic field components at the observation point changed by approximately 50% due to the presence of the copper cube. The imaginary part of the field is negligibly small for diamagnetic materials. To show the validity of the explicit formula for ferromagnetic materials, a second scenario is presented with $\sigma_\star = 0.1 \times 10^6$ (S/m) and $\mu_\star = 100 \cdot \mu_0$. The geometric configuration is reused, and the corresponding results are reported in Table III. It is shown that (27) generates the same result as the classical FEM-based approach for both the imaginary and real parts of the magnetic field.

B. Adapted EKF Model

This section describes how the EKF-based tracking approach is adapted with respect to the presented eddy current scenario. The formula given in (27) consists mainly of two parts, where the second part corrects for the effects of ferromagnetic objects. As a starting point, the first part is analyzed and given by $\int_B \nabla_{\mathbf{x}_r} G(\mathbf{x}_r, \mathbf{y}) \times \nabla_{\mathbf{y}} \times \tilde{\mathbf{H}}_a(\mathbf{y}) d\mathbf{y}$. By introducing a second coordinate frame, the integral can be simplified. The first coordinate frame is from now on called global frame and the second coordinate frame is called local frame. The local frame has its origin at the position of the first emitter. The local coordinate frame can freely move and change its orientation with respect to the global frame, which is assumed to be fixed. Consequently, the target of the tracking algorithm is the origin of the local frame expressed in the global frame. For simplicity, the volume integral over the conductive object is defined in the local coordinate frame, where its limits are constant due to the static link between the target and the object.

Furthermore, the object B is separated into a number n of smaller objects B_i with $i = 1 \ldots n$, where $B_i \subset B$ and $B_i \cap B_j = \emptyset$ with $j = 1 \ldots n$ and $i \neq j$. The volume integral can then be rewritten as

$$\int_B \nabla_{\mathbf{x}_r} G(\mathbf{x}_r, \mathbf{y}) \times \nabla_{\mathbf{y}} \times \tilde{\mathbf{H}}_a(\mathbf{y}) d\mathbf{y} = \sum_{i=1}^{n} \left(\int_{B_i} \nabla_{\mathbf{x}_r} G(\mathbf{x}_r, \mathbf{y_i}) \times \nabla_{\mathbf{y}_i} \times \tilde{\mathbf{H}}_a(\mathbf{y}_i) d\mathbf{y}_i \right). \quad (29)$$

The EKF-based tracking approach becomes applicable when $\mathbf{y_i}$ is fixed to the geometric center of B_i called $\overline{\mathbf{y}}_i$. This introduces an quantization error when calculating (27). However, as n tends to grow toward infinity and B_i shrinks toward zero, the error would vanish. As a consequence of the quantization, $\nabla_{\mathbf{x}_r} G(\mathbf{x}_r, \overline{\mathbf{y}}_i)$ becomes independent of the integration, which results in

$$\sum_{i=1}^{n} \left(\int_{B_i} \nabla_{\mathbf{x}_r} G(\mathbf{x}_r, \mathbf{y_i}) \nabla_{\mathbf{y}_i} \times \tilde{\mathbf{H}}_a(\mathbf{y}_i) d\mathbf{y}_i \right) \approx \sum_{i=1}^{n} (\nabla_{\mathbf{x}_r} G(\mathbf{x}_r, \overline{\mathbf{y}}_i) \times \int_{B_i} \nabla_{\mathbf{y}_i} \times \tilde{\mathbf{H}}_a(\mathbf{y}_i) d\mathbf{y}_i). \quad (30)$$

The integral over $\nabla_{\mathbf{y}_i} \times \tilde{\mathbf{H}}_a(\mathbf{y}_i)$ is constant and can be precomputed, which results in $\tilde{\mathbf{H}}_{C_i}$. A proper discretization for this approximation has to be found for any individual

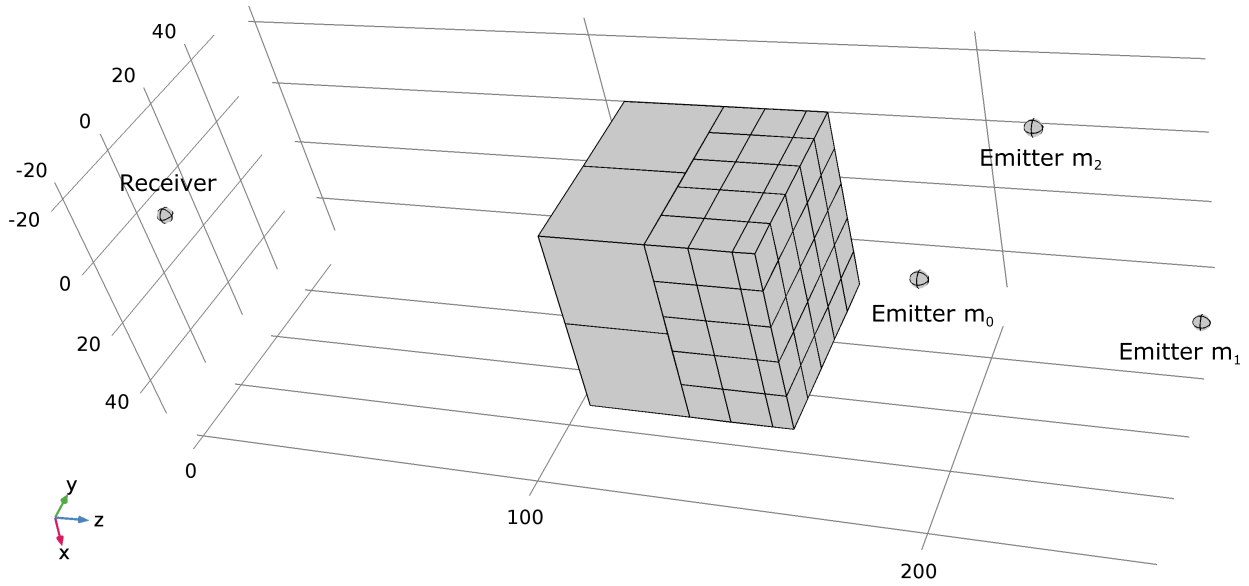

Fig. 4. Conductive object in the vicinity of the sensor is divided into smaller objects. The part that points toward the emitters is more significant. Therefore, the object resolution close to the emitters is intentionally higher. The shown constellation represents the initial state $\mathbf{X}_0$ for the vast amount of experiments throughout the article. In addition, it is used in the comparison made in Tables II and III.

object geometry and constellation with respect to the emitters. The used discretization for the copper cube is schematically shown in Fig. 4. The parts of the cube, which are closer to the emitters, are more significant. Therefore, the surface with higher object resolution points toward the emitter. A higher object resolution would increase the accuracy of (30) and is, therefore, favorable. However, this comes with additional computational cost.

The described procedure is also applied to the second part of the formula. On the contrary, the integral over the magnetic field instead of the curl of the magnetic field is required to be precomputed. In total, for large n and small B_i, a good approximation of (27) is given by

$$\tilde{\mathbf{H}}_a(\mathbf{x}_r) \approx \sum_{i=1}^{n} (\nabla_{\mathbf{x}_r} G(\mathbf{x}_r, \overline{\mathbf{y}}_i) \times \tilde{\mathbf{H}}_{C_i}) + \left(1 - \frac{\mu_\star}{\mu_0}\right) \sum_{i=1}^{n} (\mathbf{H}_i \cdot \nabla_{\overline{\mathbf{y}}_i}) \nabla_{\mathbf{x}_r} G(\mathbf{x}_r, \overline{\mathbf{y}}_i). \quad (31)$$

Here, $\mathbf{H}_i$ denotes the volume integral over the magnetic field in B_i in the presence of the object. In the global frame, the quantity $\overline{\mathbf{y}}_i$ can be expressed as $\overline{\mathbf{y}}_i = \mathbf{r} + \mathbf{R}\mathbf{z}_i$ with $\mathbf{z}_i$ being the known distance (in local frame) between the emitter and the geometric center of B_i. Note that the known point of observation $\mathbf{x}_r$ is defined in the global coordinate system, which result in six remaining DOF, i.e., $\mathbf{x}_s$ and $\boldsymbol{\theta}$.

The geometric dependences are schematically visualized in Fig. 5. Although Fig. 5 shows a 2-D setup, the same relations hold for the 3-D case. The magnetic field at $\mathbf{x}_r$ is ultimately given by

$$\mathbf{H}(\mathbf{x}_r) = \mathbf{H}_0(\mathbf{r}, \mathbf{m}) + \tilde{\mathbf{H}}_a(\mathbf{x}_r). \quad (32)$$

Note that (31) explicitly expresses the change of magnetic field at observation point $\mathbf{x}_r$ without solving the full Maxwell's equations. Since the position and orientation of the target change over time, the result needs continuously to be updated. FEM-based solutions, for example, are computationally heavy and can hardly be solved in real time on common hardware. The introduced concept in contrast is computationally lightweight and can easily be evaluated at certain instances in time. The approximation made from (30) to (31) limits the accuracy. The algorithm cost directly depends on the number of subobjects B_i. For complex and

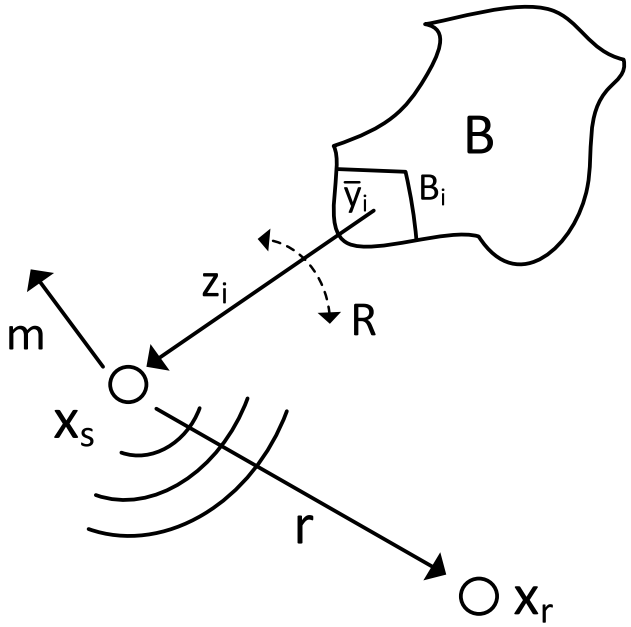

Fig. 5. Geometric dependences are schematically shown. Here, $\mathbf{x}_r$ represents the point of observation defined in global coordinate system and $\mathbf{x}_s$ represents the magnetic field source and origin of the local coordinate frame. Furthermore, $\mathbf{z}_i$ given in local frame denotes the vector between the geometric center of object part B_i and magnetic field source. The limits of object B are known in local frame. The transition between the local and the global coordinate frame is defined by translation $\mathbf{r}$ and rotation $\mathbf{R}$.

large shapes, it can be difficult to get accurate results with a low object resolution. In fact, it is a tradeoff between accuracy and computational complexity. The nonlinear function $\mathbf{h}$ in the observation equation (14) clearly corresponds now to (32). To apply the EKF, it needs to be linearized with respect to the system states $\mathbf{X}_t$.

C. Tracking Experiments

This section compares the EKF-based tracking performance of the model extended for close conductive objects (32) with the model given by (1). Note that a conductive cube, shown in Fig. 4, is located close to the magnetic field sources. Most of the used parameters of this experiments are reused from Section III-C. The starting point of the trajectory $\mathbf{X}_0$, shown in Fig. 4, is given by

$$\mathbf{v}_0 = [0.001,\ 0.001,\ 0.001]^T, \quad \mathbf{z}_0 = [0,\ 0,\ 0.2]^T$$
$$\boldsymbol{\omega}_0 = [0,\ 0,\ 0]^T, \quad \boldsymbol{\theta}_0 = [0,\ 0,\ 0]^T.$$

To get a meaningful comparison, the initial guess of the EKF is equal to the initial position $\hat{\mathbf{X}}_0 = \mathbf{X}_0$. For this and the following experiments with good initial guess, the state propagation covariance is lowered to $10^{-3} \cdot \mathbf{I}$ due to the good initial guess. The process and measurement noise covariances are reused from the previous experiment. The edge length of the conductive cube B is 5 cm and its center is located at $[0,\ 0,\ 0.15]^T$. The geometry is separated into $n = 79$ smaller cubes B_i, as shown in Fig. 4. The integrals over the curl of the magnetic field resulting in $\tilde{\mathbf{H}}_{C_i}$ and the integrals over the magnetic field resulting in $\mathbf{H}_i$ are precomputed. For zero conductivity and permeability, the models $\mathbf{H}_0$ and $\mathbf{H}$ have the same result.

First, a comparison is made, where the conductivity of the cube is changed to $\sigma_\star = 1000$ (S/m), which is approximately the conductivity of various carbon-based materials.

The estimated trajectory and orientation using both the models as well as the true trajectory and true orientation are reported in Figs. 6 and 7, respectively. It is observable that, for the used conductivity, the performance of both the models is acceptable. The trajectory and orientation of the target is well tracked. The experiment is repeated a hundred times and the average mse for different measurement noise levels is reported in Table IV. It is shown that, for objects with low conductivity, the interference is very small and the model extension can be omitted for the presented case. Depending on the shape of the object, its conductivity, and the desired accuracy, it can individually be decided whether the extension is required or not.

To visualize the advantages of the $\mathbf{H}$ model, the conductivity of B is increased to the level of copper $\sigma_\star = 59.9 \times 10^6$ (S/m). The evolution of the position and orientation estimates using both the models is reported in Figs. 8 and 9, respectively. The EKF tracking accuracy based on the $\mathbf{H}_0$ model decreased dramatically, while for the adapted model $\mathbf{H}$, the tracking remains accurate. Here, the benefit in terms of accuracy of the comparatively complex model extension is clearly visible. The extended model is able to accurately track the trajectories until the receiver signal strength becomes too weak and measurement noise starts to dominate. The base model, which neglects the highly conductive cube, performs insufficient even in the areas, where the receiver signal strength is still reasonable. As in the previous experiments, the mse is carried out and shown in Table V. For the highly conductive cube, the superior performance of the extended model is also pronounced by the mse.

A third experiment featuring a ferromagnetic material with parameters $\sigma_\star = 0.1 \times 10^6$ S/m and $\mu_\star = 100 \cdot \mu_0$ is carried out. In Figs. 10 and 11, it is shown that the tracking performance is maintained for ferromagnetic objects. As in the previous experiments, the MSE is carried out and shown

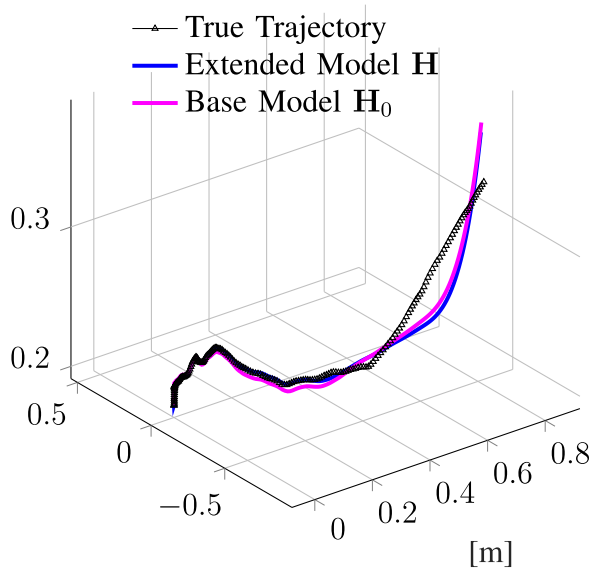

Fig. 6. EKF-based position tracking is shown with two different underlying models. The black markers indicate the true position, the magenta waveform represents the underlying model (1), whereas the blue waveform shows the tracking based on the extended model (32). Due to the low conductivity of the object ($\sigma_\star = 1000$ S/m), the accuracy of both the models is almost equal.

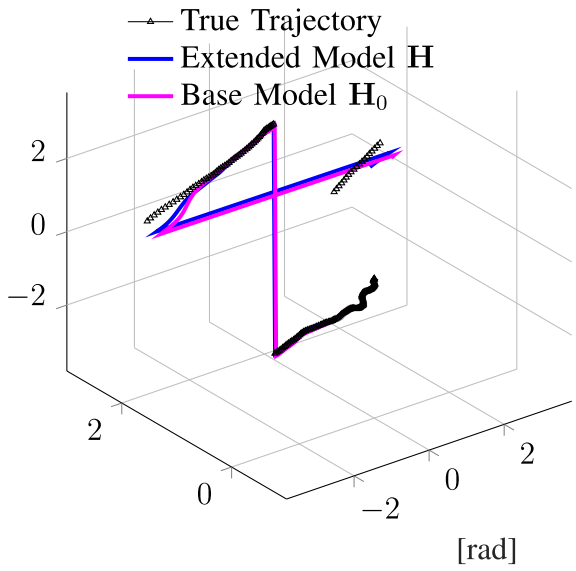

Fig. 7. EKF-based orientation tracking is shown with two different underlying models. The waveform colors and underlying models are defined as in Fig. 6. Due to the low conductivity of the object ($\sigma_\star = 1000$ S/m), the accuracy of both the models is almost equal.

TABLE IV
MSE IS CARRIED OUT FOR DIFFERENT MEASUREMENT NOISE LEVELS AND BOTH UNDERLYING MODELS

Measurement Noise Variance σ^2 ($\frac{\mathrm{A}^2}{\mathrm{m}^2}$)	10^{-1}	10^{-2}	10^{-3}	10^{-4}	10^{-5}
MSE Extended Model $\mathbf{H}$ (m^2)	0.1214	0.0526	0.0091	0.0042	0.0009
MSE Base Model $\mathbf{H}_0$ (m^2)	0.1236	0.0534	0.0094	0.0048	0.0010

TABLE V
MSE IS CARRIED OUT FOR DIFFERENT MEASUREMENT NOISE LEVELS AND BOTH UNDERLYING MODELS

Measurement Noise Variance σ^2 ($\frac{\mathrm{A}^2}{\mathrm{m}^2}$)	10^{-1}	10^{-2}	10^{-3}	10^{-4}	10^{-5}
MSE Extended Model $\mathbf{H}$ (m^2)	0.073	0.0296	0.0114	0.0036	0.0009
MSE Base Model $\mathbf{H}_0$ (m^2)	0.1296	0.1318	0.0911	0.0773	0.0641

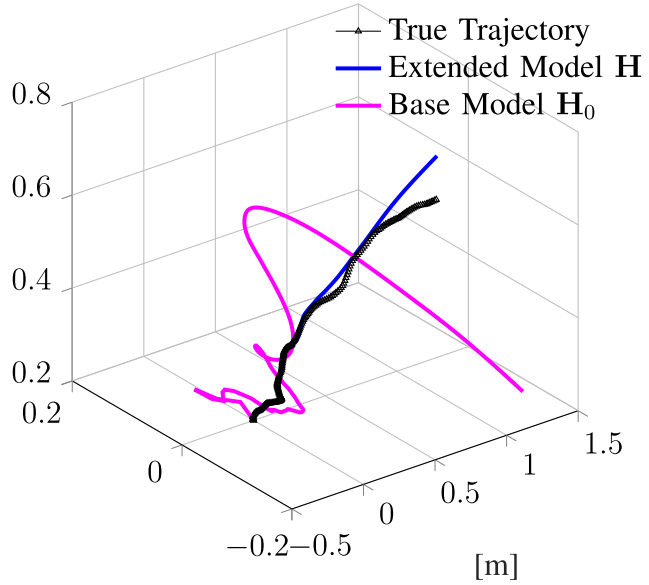

Fig. 8. EKF-based position tracking is shown with two different underlying models. The black markers indicate the true position, the magenta waveform represents the underlying model (1), which holds for surrounding air, whereas the blue waveform shows the superior tracking performance based on the extended model (32) for close-by conductive objects. The conductivity of the cube is $\sigma_\star = 59.9 \times 10^6$ S/m.

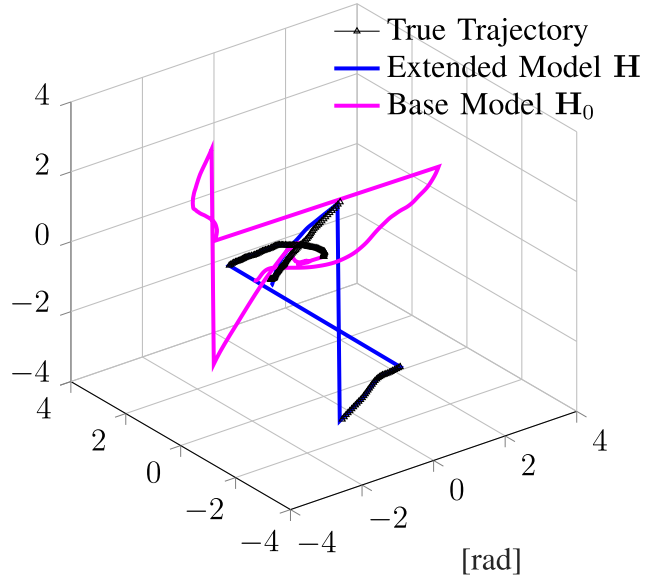

Fig. 9. EKF-based orientation tracking is shown with two different underlying models. The waveform colors and underlying models are defined as in Fig. 8. Due to the high conductivity of the object ($\sigma_\star = 59.9 \times 10^6$ S/m), the extended model performs superior.

in Table VI. Note that the introduced phase shift, also shown in Table III, may be difficult to measure with common sensors. However, it can easily be estimated when the emitter and the receiver are synchronized. A comparison with the traditional model (1) is neglected, because it does not support the phase shift introduced by the ferromagnetic material. For certain constellations, the phase shift is substantial. As a consequence, the EKF based on the traditional model diverges quickly.

In the last experiment, a trajectory, which is not randomly generated, is used. Instead of using the Brownian motion model from (8), a helical line with constant vertical velocity is used. In addition, the angular velocity is constant, but its x and y components vary periodically. Note that the attitude of the target is always aligned to the flight direction. The system model remains the same and is designed for random trajectories. The flight path simulates nonrandom real-world movement, e.g., a UAV in the vicinity of the sensor. The initial states $\mathbf{X}_0$ are given by

$$\mathbf{v}_0 = [0,\ 0.12,\ 0.02]^T, \quad \mathbf{z}_0 = [0.6,\ 0,\ 0]^T$$
$$\boldsymbol{\omega}_0 = [0,\ 0,\ 0.02]^T, \quad \boldsymbol{\theta}_0 = [0.1662,\ 0,\ 0.02]^T.$$

The initial guess of the EKF is $\hat{\mathbf{X}}_0 = \mathbf{X}_0$. The conductive cube is made of copper with 59.9×10^6 S/m and $\mu_\star = \mu_0$. Its relative location and size is reused from the previous experiments. The simulated flight lasts 80 s, and its trajectory is given by

$$z(t) = \begin{bmatrix} 0.6\cos(0.2\ t) \\ 0.6\sin(0.2\ t) \\ 0.01\ t \end{bmatrix}, \quad \boldsymbol{\theta}(t) = \begin{bmatrix} 0.0831 \\ 0 \\ 0.02\ t \end{bmatrix}. \tag{33}$$

The evolution of the position and orientation estimates is shown in Figs. 12 and 13, respectively. Again, the mse is carried out for five different measurement noise levels and is shown in Table VII. The experiment is repeated a 100 times each, using the same trajectory but different realizations of the noise distribution. The estimator with an underlying extended

TABLE VI
MSE IS CARRIED OUT FOR DIFFERENT MEASUREMENT NOISE LEVELS AND BOTH UNDERLYING MODELS

Measurement Noise Variance σ^2 $(\frac{\mathrm{A}^2}{\mathrm{m}^2})$	10^{-1}	10^{-2}	10^{-3}	10^{-4}	10^{-5}
MSE Extended Model $\mathbf{H}$ (m^2)	0.0980	0.0353	0.0066	0.0054	0.0014

TABLE VII
MSE IS CARRIED OUT FOR DIFFERENT MEASUREMENT NOISE LEVELS AND BOTH UNDERLYING MODELS

Measurement Noise Variance σ^2 $(\frac{\mathrm{A}^2}{\mathrm{m}^2})$	10^{-1}	10^{-2}	10^{-3}	10^{-4}	10^{-5}
MSE Extended Model $\mathbf{H}$ (m^2)	0.1214	0.0526	0.0091	0.0042	0.0009
MSE Base Model $\mathbf{H}_0$ (m^2)	0.1236	0.0534	0.0094	0.0048	0.0010

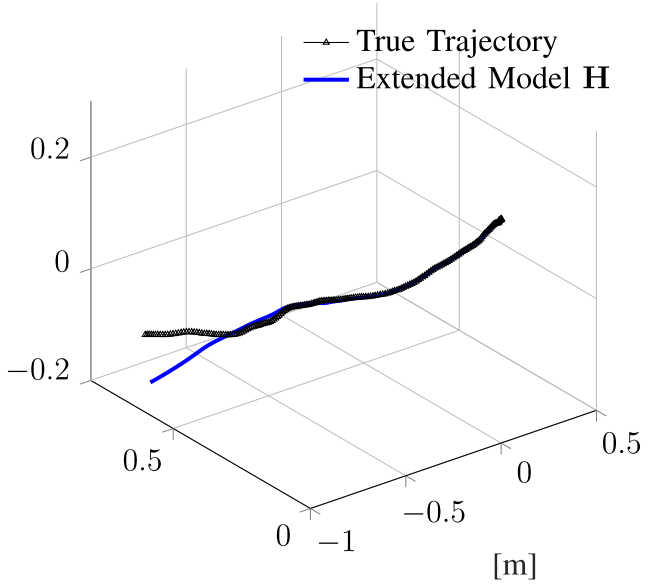

Fig. 10. Black markers indicate the true position and the blue waveform represents the EKF-based position tracking for the extended model (32), which holds for close-by conductive and ferromagnetic materials. The conductivity and permeability of the cube are $\sigma_\star = 0.1 \times 10^6$ S/m and $\mu_\star = 100 \cdot \mu_0$, respectively.

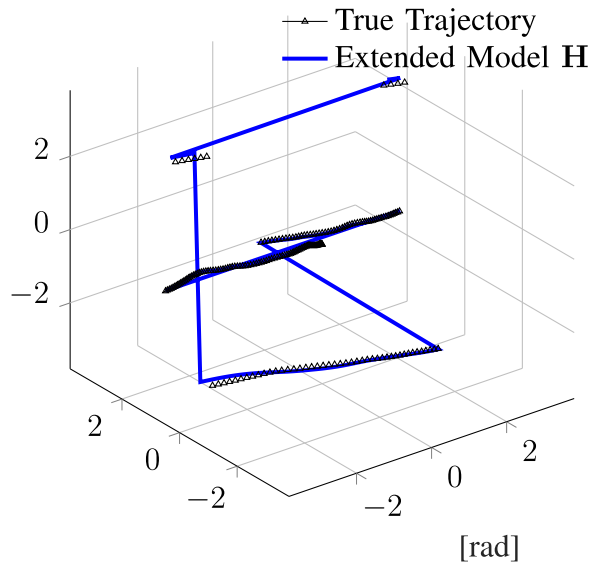

Fig. 11. Black markers indicate the true orientation and the blue waveform represents the EKF-based orientation tracking for the extended model (32), which holds for close-by conductive and ferromagnetic materials. The conductivity and permeability of the cube is $\sigma_\star = 0.1 \times 10^6$ S/m and $\mu_\star = 100 \cdot \mu_0$, respectively.

model accurately tracks the nonrandom helical trajectory until the received signal strength becomes weak caused by the increasing distance to the transmitter. The traditional model in contrast only roughly tracks the helical line. It is shown that the approach of generally modeling movement using Brownian motion is also valid for nonrandom trajectories. Targets such as wheeled robots or UAVs are commonly modeled using their specific dynamics. This technique in contrast can be used without prior knowledge about the robot-actuation properties. Throughout the article, it is shown that the sensor performance increases with the decreasing distance to the receiver, e.g., base station. This makes it especially useful to support autonomous landing scenarios under harsh conditions of UAVs. Often, fiducial markers are used to support autonomous landing maneuvers. Detrimental influences such as rain, snow, fog, or bad illumination limit the usability of those markers. In contrast, such circumstances do not influence the performance of the proposed sensor system. It is suggested to use it complementary to existing techniques, e.g., VIO.

D. Computational Complexity

This section gives an idea of the computational complexity of the algorithm. The complexity is mainly determined by the number of subobjects B_i. The more the subobjects, the better the accuracy of the algorithm. In fact, it is a tradeoff between accuracy and computational complexity. For the presented case with the conductive/ferromagnetic cube consisting of 79 subobjects, the computation times are carried out. The computation was performed in MATLAB running on a notebook with an Intel i7-7600U processor. The memory requirements are negligibly small. A pose-estimation iteration using the presented EKF framework requires 2.5 ms for nonconductive/non ferromagnetic objects. This represents the least complex case, where the model extension is not required. For the conductive but nonferromagnetic cube (see Figs. 8 and 9), the computation time is 20 ms. Finally, for a conductive as well as ferromagnetic cube (see Figs. 10 and 11), the computation time is about 200 ms. It can be concluded that the algorithm is very fast for conductive but nonferromagnetic

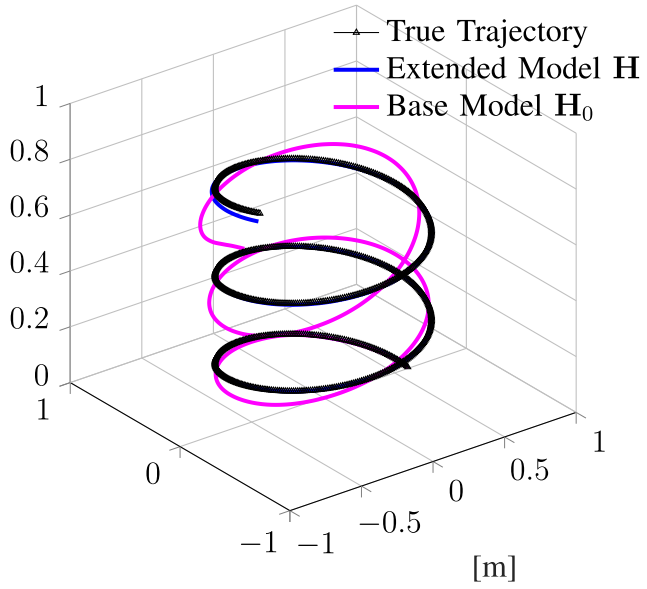

Fig. 12. EKF-based position tracking is shown with two different underlying models. The black markers indicate the true position, the magenta waveform represents the underlying model (1), whereas the blue waveform shows the tracking based on the extended model (32). The conductivity of the close-by copper cube is $\sigma_\star = 59.9 \times 10^6$ S/m. The used trajectory is not randomly chosen, despite the model formulation that expects random motion.

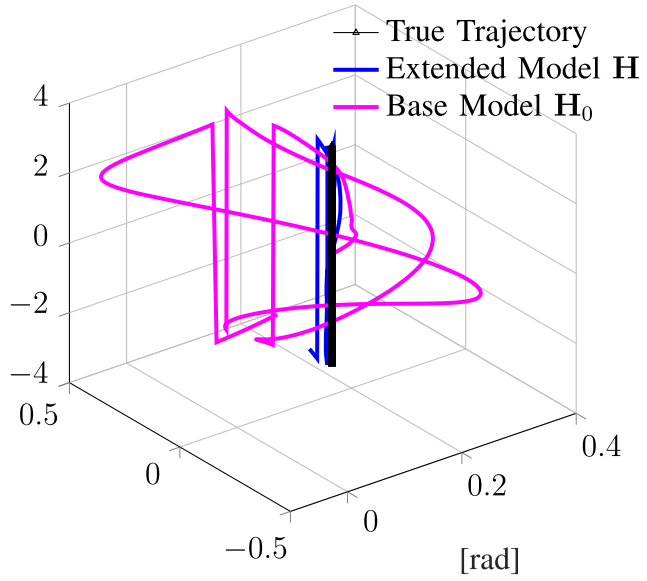

Fig. 13. EKF-based position tracking is shown with two different underlying models. The black markers indicate the true position, the magenta waveform represents the underlying model (1), whereas the blue waveform shows the tracking based on the extended model (32). The conductivity of the close-by copper cube is $\sigma_\star = 59.9 \times 10^6$ S/m. The used trajectory is not randomly chosen, despite the model formulation that expects random motion.

materials and can consequently be used in many applications. Typical materials are water, carbon, aluminum, or copper. For the ferromagnetic materials, the computation times are higher, but there are still applicable scenarios, e.g., complementary to other pose-estimation principles. The conducted computation times show the benefit with respect to classical FEM-based approaches. The FEM environment used in Tables II and III requires 95 s and additionally 3.5 GB of memory for a single forward calculation of the electromagnetic field. Such an update rate is too low even for slowly moving objects.

V. Conclusion

In this article, a 6-DOF pose-estimation principle based on electromagnetic fields is presented. It is especially useful for autonomous systems operating under harsh conditions such as denied line of sight, bad light conditions, rain, fog, or when navigating close to objects. The system consists of two parts, a transmitter and a receiver with known pose. The pose of the transmitter, which is, e.g., mounted on a mobile platform, is estimated. The system accuracy increases with the decreasing distance, which makes it especially beneficial to the landing scenarios of UAVs. This article additionally introduces a methodology to account for conductive and ferromagnetic objects in the vicinity of the sensor, which alters the electromagnetic field due to eddy currents. The correctness of the introduced formulation is verified by comparing it with an FEM-based solution of the full Maxwell equations. FEM-based solutions are computationally complex and require a huge amount of memory. Thus, recalculating the FEM solution for each step in a pose-tracking scene is inappropriate for real-time applications. In contrast, the introduced model is computationally lightweight. It only requires a single FEM-based field solution, which can be precomputed. The consecutive field updates are analytically evaluated. The applicability for real-time pose tracking is showcased by carrying out the computation times of an employed EKF. In addition, the introduced model is compared with the traditional magnetic field model, and the superior performance of the model extension in the interference scenarios is reported.

References

[1] M. Bloesch, M. Burri, S. Omari, M. Hutter, and R. Siegwart, "Iterated extended Kalman filter based visual-inertial odometry using direct photometric feedback," *Int. J. Robot. Res.*, vol. 36, no. 10, pp. 1053–1072, 2017.

[2] K. Hausman, S. Weiss, R. Brockers, L. Matthies, and G. Sukhatme, "Self-calibrating multi-sensor fusion with probabilistic measurement validation for seamless sensor switching on a UAV," in *Proc. IEEE Int. Conf. Robot. Automat. (ICRA)*, May 2016, pp. 4289–4296. doi: 10.1109/ICRA.2016.7487626.

[3] M. Heydariaan, H. Mohammadmoradi, and O. Gnawali, "Toward standard non-line-of-sight benchmarking of ultra-wideband radio-based localization," in *Proc. IEEE Workshop Benchmarking Cyber-Phys. Netw. Syst. (CPSBench)*, Apr. 2018, pp. 19–24. doi: 10.1109/CPS-Bench.2018.00010.

[4] C. Zhang, M. J. Kuhn, B. C. Merkl, A. E. Fathy, and M. R. Mahfouz, "Real-time noncoherent UWB positioning radar with millimeter range accuracy: Theory and experiment," *IEEE Trans. Microw. Theory Techn.*, vol. 58, no. 1, pp. 9–20, Jan. 2010.

[5] X. Yun, E. R. Bachmann, and R. B. Mcghee, "A simplified quaternion-based algorithm for orientation estimation from earth gravity and magnetic field measurements," *IEEE Trans. Instrum. Meas.*, vol. 57, no. 3, pp. 638–650, Mar. 2008.

[6] T. Schlegl, M. Neumayer, S. Mühlbacher-Karrer, and H. Zangl, "A pretouch sensing system for a robot grasper using magnetic and capacitive sensors," *IEEE Trans. Instrum. Meas.*, vol. 62, no. 5, pp. 1299–1307, May 2013.

[7] T. D. Than, G. Alici, H. Zhou, and W. Li, "A review of localization systems for robotic endoscopic capsules," *IEEE Trans. Biomed. Eng.*, vol. 59, no. 9, pp. 2387–2399, Sep. 2012.

[8] H. Gietler, C. Böhm, T. Mitterer, L.-M. Faller, S. Weiss, and H. Zangl, "4-DOF magnetic field based localization for UAV navigation," in *Proc. Int. Symp. Exp. Robot. (ISER)*, Buenos Aires, Argentina, Nov. 2018, pp. 5–8.

[9] T. Mitterer, H. Gietler, L.-M. Faller, and H. Zangl, "Artificial landmarks for trusted localization of autonomous vehicles based on magnetic sensors," *Sensors*, vol. 19, no. 4, p. 813, 2019.
[10] H. Ammari, J. Chen, Z. Chen, J. Garnier, and D. Volkov, "Target detection and characterization from electromagnetic induction data," *J. Math. Pures Appl.*, vol. 101, no. 1, pp. 54–75, 2014.
[11] J. D. Jackson, *Classical Electrodynamics*, 3rd ed. New York, NY, USA: Wiley, 1999. [Online]. Available: http://cdsweb.cern.ch/record/490457
[12] J. E. Green, D. A. Stone, M. P. Foster, and A. Tennant, "Spatially resolved measurements of magnetic fields applied to current distribution problems in batteries," *IEEE Trans. Instrum. Meas.*, vol. 64, no. 4, pp. 951–958, Apr. 2015.
[13] H. A. Jaeger and P. Cantillon-Murphy, "Electromagnetic tracking using modular, tiled field generators," *IEEE Trans. Instrum. Meas.*, to be published.
[14] H.-Y. Wei and A. J. Wilkinson, "Design of a sensor coil and measurement electronics for magnetic induction tomography," *IEEE Trans. Instrum. Meas.*, vol. 60, no. 12, pp. 3853–3859, Dec. 2011.
[15] A. R. Silva and M. Moghaddam, "Design and implementation of low-power and mid-range magnetic-induction-based wireless underground sensor networks," *IEEE Trans. Instrum. Meas.*, vol. 65, no. 4, pp. 821–835, Apr. 2016.
[16] L. C. Evans, *An Introduction to Stochastic Differential Equations*. Providence, RI, USA: AMS, 2012.
[17] H.-H. Kuo, *Introduction to Stochastic Integration*. New York, NY, USA: Springer, 2006.
[18] H. Ammari *et al.*, *Mathematical and Statistical Methods for Multistatic Imaging* (Lecture Notes in Mathematics), vol. 2098. Cham, Switzerland: Springer, 2013.
[19] H. Ammari, T. Boulier, J. Garnier, H. Kang, and H. Wang, "Tracking of a mobile target using generalized polarization tensors," *SIAM J. Imag. Sci.*, vol. 6, no. 3, pp. 1477–1498, 2013.
[20] *COMSOL Multiphysics V.5.2a*, COMSOL AB, Stockholm, Sweden, 2019. [Online]. Available: https://www.comsol.com

Harald Gietler was born in Villach, Austria. He received the B.Sc. and Dipl.Ing. degrees in information technology from the University of Klagenfurt, Klagenfurt, Austria, in 2015 and 2017, respectively, where he is currently pursuing the Ph.D. degree in electrical engineering.

From 2015 to 2017, he was with Infineon Technologies, Villach, Austria, where he focused on system identification and digital self-tuning control for dc–dc converters. In 2017, he joined the University of Klagenfurt. His current research interests include computational electromagnetics, sensor technologies, power converters, and system identification.

Habib Ammari received the bachelor's, master's, and Ph.D. degrees in applied mathematics from the École Polytechnique, Palaiseau, France, in 1992, 1993, and 1995, respectively, and the Habilitation degree in mathematics from the University of Pierre and Marie Curie, Paris, France, in 1998.

Before moving to ETH, he was the Director of Research with the Department of Mathematics and Applications, École Normale Supérieure, Paris. He is currently a Professor of applied mathematics with ETH Zürich, Zürich, Switzerland. He is also a world leading expert in wave propagation phenomena in complex media, mathematical modeling in photonics and phononics, and mathematical biomedical imaging. He has advised 34 Ph.D. students and 23 post-doctoral researchers. He has published more than 200 research articles, eight high-profile research-oriented books, and edited eight books on contemporary issues in applied mathematics.

Dr. Ammari was a recipient of several international prizes. He is also listed as an ISI Highly Cited Researcher.

Hubert Zangl received the Dipl.Ing. degree in telematics, the Dr.Tech. degree in electrical engineering, and the Venia Docendi degree in sensors and instrumentation from the Graz University of Technology (TUG), Graz, Austria, in 2001, 2005, and 2009, respectively.

From 2010 to 2013, he was an Associate Professor in sensors and instrumentation with the Institute of Electrical Measurement and Measurement Signal Processing, TUG. Since September 2013, he has been a Professor of sensors and actuators with the Institute of Smart System Technologies, University of Klagenfurt, Klagenfurt, Austria. His current research interests include design and optimization of smart sensors and actuators, robustness and reliability of sensors and actuators, sensor signal processing, autarkic wireless sensors, energy harvesting and applications in robot sensing, and the Internet of Things (IoT).